Halide Heterogeneous Structure Boosting Ionic Diffusion and High-Voltage Stability of Sodium Superionic Conductors

Jiamin Fu[1,2†], Shuo Wang[3†], Duojie Wu[4†], Jing Luo[1], Changhong Wang[4], Jianwen Liang[1], Xiaoting Lin[1], Yang Hu[1], Shumin Zhang[1,2], Feipeng Zhao[1], Weihan Li[1], Minsi Li[1], Hui Duan[1], Yang Zhao[1], Meng Gu[4*], Tsun-Kong Sham[2*], Yifei Mo[3*], Xueliang Sun[1,4*]

[1] Department of Mechanical and Materials Engineering, University of Western Ontario, London, Ontario, N6A 5B9, Canada

[2] Department of Chemistry, University of Western Ontario, London, Ontario, N6A 5B7, Canada

[3] Department of Materials Science and Engineering, University of Maryland, College Park, MD 20742, USA.

[4] Eastern Institute for Advanced Study, Eastern Institute of Technology, Ningbo, Zhejiang 315200, P. R. China

[5] Canadian Light Source Inc., University of Saskatchewan, Saskatoon, Saskatchewan, S7N 2V3, Canada

[†] These authors contributed equally to this work

* Corresponding authors: tsham@uwo.ca; yfmo@umd.edu; xsun9@uwo.ca

Abstract:

The development of solid-state sodium-ion batteries (SSSBs) heavily hinges on the development of a Na^+ conductor (SSC) that features high conductivity, (electro)chemical stability, and deformability. The construction of heterogeneous structures offers a promising approach to comprehensively enhancing these properties in a way that differs from traditional structural optimization. Here, we exploit the structural variance between high- and low-coordination halide frameworks to develop a new class of halide heterogeneous structure electrolytes (HSEs). The halide HSEs incorporating a UCl_3-type high-coordination framework and amorphous low-coordination phase achieved the highest Na^+ conductivity (2.7 mS cm^{-1} at room temperature) among halide SSCs so far. By discerning the individual contribution of the crystalline bulk, amorphous region, and interface, we unravel the synergistic ion conduction within halide HSEs and provide a comprehensive explanation of the amorphization effect. More importantly, the excellent deformability, high-voltage stability, and expandability of HSEs enable effective SSSB integration. Using a cold-pressed cathode electrode composite of uncoated $Na_{0.85}Mn_{0.5}Ni_{0.4}Fe_{0.1}O_2$ and HSEs, the SSSBs present stable cycle performance with a capacity retention of 91.0 % after 100 cycles at 0.2 C.

Keywords: solid-state electrolyte, heterogeneous structure, composites, UCl_3-type framework, Na^+ diffusion.

Introduction

Given the growing scarcity of lithium resources, solid-state sodium-ion batteries (SSSBs) have garnered significant attention owing to their sustainable composition, high theoretical energy density, and inherent safety advantages.[1-3] However, the development of solid-state sodium-ion batteries (SSSBs) imposes stringent requirements on superionic Na-ion conductors (SSCs), including high ionic conductivity (> 1 mS cm^{-1}) at room temperature (RT), excellent deformability for intimate solid-solid contact, and exceptional interfacial stability with electrode materials, yet no single SSC currently fulfills all these requirements simultaneously.[4-6] Among several categories of SSCs, inorganic oxide SSCs[7,8] show higher Na-ion conductivity of ~ 1 mS cm^{-1} and better electrochemical stability than that of polymer-based SSCs, but their rigid nature makes them extremely challenging to maintain tight inter-particle contact in SSSBs.[1] Furthermore, closo-borates[9], sodium thiophosphates[10,11], and their analogues[12-17] emerged in recent years due to their deformability and exceptional ionic conductivity (up to the level of 10 mS cm^{-1}). Nevertheless, their limited oxidative stability hinders them from reaching competitive energy densities with high-voltage cathodes.

Recently, the successful discovery of a range of Li-ion halide conductors[18-26], which exhibit good deformability, high ionic conductivity, and (electro)chemical stability, has inspired research into sodium halide analogues as potential SSCs. However, due to the disparity in ionic radius between Li (76 pm) and Na (> 100 pm), the design principles for superionic lithium conductors cannot be directly applied to SSCs. As a result, the reported halide-based SSCs generally exhibit insufficient ionic conductivity. For instance, the trigonal structured Na_2ZrCl_6[27] and its aliovalent substitution $Na_{3-x}Er_{1-x}Zr_xCl_6$[28] and $Na_{3-x}Y_{1-x}Zr_xCl_6$[29] present Na^+ ionic conductivities of 0.018 mS cm^{-1} (30 °C), 0.04 mS cm^{-1} (25 °C), and 0.066 mS cm^{-1} (20 °C), respectively. Phillip Ridley et al.[30] further increased the RT ionic conductivity of $Na_xY_{0.25}Zr_{0.75}Cl_{3.75+x}$ to 0.4 mS cm^{-1} by reducing the NaCl content and transitioning to an amorphous state. The authors suggest that the bigger free volume and higher number of Na^+ vacancies in the amorphous state likely account for the high ionic conductivity. However, no halide SSC has achieved an ionic

conductivity above 1 mS cm^{-1} as comparable to the lithium analogues.

The construction of heterogeneous structures offers an alternative approach to enhancing ion conduction distinct from traditional structural optimization.[31] Hiram Kwak et al.[32] recently reported an intriguing finding of improving the Na^+ conductivity of 0.011 mS cm^{-1} for Na_2ZrCl_6 to 0.11 mS cm^{-1} for ZrO_2-Na_2ZrCl_6 even if the bulk ZrO_2 is not conductive. Similarly, an increase in ionic conductivity by one to two orders of magnitude has frequently been observed in various heterostructure systems, such as crystal-crystal (LiI·Al_2O_3[33], LiI·Li_3PO_4[34], and Li_2ZrCl_6·ZrO_2[32]), crystal-glass (AgI·Ag_3BO_3[35], P_2S_5·Li_2S·LiI[36], and $LiBH_4$·fumed silica[37]), and polymer-inorganic (PEO·Al_2O_3[38] and PEO·$Li_7La_3Zr_2O_{12}$[39]), which are usually attributed to the effect of space charge layer at the interface.[31] However, the exploration of halide heterogeneous-structure electrolytes (HSE) as potential SSCs is still on the way, and there remains a lack of clarity regarding the specific roles of heterogeneous components on ionic conductivity.

Besides the common close-packed anion structures of Li^+ superionic conductors, we have lately proposed another group of UCl_3-type frameworks[40], in which highly distorted octahedral sites constitutes a fast one-dimensional (1D) diffusion channel for Li^+/Na^+ hopping. However, the limitation of 1D transport characteristics restricts its macroscopic ionic conductivity across mismatched grains. Yi-Chen Yin et al.[41] take advantage of high-valence cationic doping to obtain three-dimensional (3D) transport within the single structure, leading to a high Li^+ ionic conductivity of 3.02 mS cm^{-1} at 30 °C. When the UCl_3-type lattice maintains the fast 1D channels without aliovalent substitution, we found that the UCl_3-type lattice possesses an appealing capability to induce amorphization in surrounding low-coordination halides, creating interparticle conduction buffers to achieve fast macroscopic ion diffusion.[40] These behaviors fulfill the key focuses of HSEs development, including the sustained structural integrity of each component and fast ion diffusion in the different components. Hence, incorporating UCl_3-type frameworks into halide HSEs represents a promising strategy for effectively exploiting the rapid 1D diffusion and amorphization capabilities inherent to the UCl_3-type framework, thereby enhancing Na^+ ion conductivity synergistically.

In this study, we delve into the structural characteristics of polycationic halides that incorporate the UCl_3-type frameworks and different ternary metal halides. By exploiting the structural variances between high- and low-coordination halide frameworks, we have developed a novel class of halide HSEs that exhibit an outstanding ionic conductivity of up to 2.7 mS cm^{-1}. This achievement marks the highest value recorded among halide SSCs to date. The heterogeneous structures of the HSEs were identified by the X-ray diffraction (XRD), pair distribution function (PDF), high-resolution transmission electron microscopy (HRTEM), and extended X-ray absorption fine structure (EXAFS). By combining *ab initio* molecular dynamics (AIMD) simulations with low-temperature electrochemical impedance fittings, we clarified the individual contributions of the crystalline bulk, amorphous region, and interface to ionic conductivity. Notably, we distinctly highlighted the substantial role of the amorphization effect in this context. Furthermore, the halide HSEs demonstrated excellent deformability, high-voltage stability, and expandability. The cold-pressed composite using uncoated $Na_{0.85}Mn_{0.5}Ni_{0.4}Fe_{0.1}O_2$ (NMNFO) and HSEs presented stable cycle performance with a capacity retention of 91.0 % after 100 cycles at 0.2 C in SSSBs, outperforming that of using Na_3PS_4 as catholyte. The composition of halide HSEs is highly designable and extendable, allowing for a tunable cathode-electrolyte interphase (CEI) design for different cathode materials and requirements.

Results and discussion

Construction and characterization of halide heterostructures

Two types of sodium metal ternary halides, categorized based on the distinct metal-halogen coordination numbers (CN), were mechanochemically synthesized in this study: **1. High coordination frameworks (HCF, CN > 6)**, represented by UCl_3-type $Na_{3x}M_{2-x}Cl_6$ (M = La, Sm). **Fig. 1a-b** presents the Rietveld refinements of XRD patterns of $Na_{0.75}Sm_{1.75}Cl_6$ (HCF-Sm) and $Na_{0.75}La_{1.75}Cl_6$ (HCF-La). HCF-Sm and HCF-La are constituted by $[MCl_9]^{6-}$ tricapped trigonal prism with Na atoms partially occupying Wyckoff

sites *2b* (octahedral sites) and *2c* (La, Sm sites), as shown in **Fig. 1d**. In the UCl_3-type structure, the AIMD simulations revealed fast Na^+ conduction in the numerous of face-sharing distorted octahedra sites along the *c*-axis (**Fig. S1a-b**). **2. Low coordination frameworks (LCF, CN ≤ 6)** represented by dispersed $[MCl_6]^{x-}$ octahedra, such as $NaTaCl_6$ (LCF-Ta). According to the Rietveld refinements of XRD pattern (**Fig. 1c**), the crystalline LCF-Ta comprises an $[TaCl_6]^-$ octahedral framework located at the corners of the unit cell ($P2_1/c$) edge-sharing by two $[NaCl_7]^{6-}$ capped trigonal prism (**Fig. 1e**). Different from the UCl_3-type structure, Na^+ ions in LCF-Ta are confined at equilibrium sites surrounding by orderly distributed $[TaCl_6]^-$ octahedra as depicted in AIMD simulations (**Fig. S1c**). The formation of a 3D diffusional network in LCF-Ta requires overcoming a substantial activation energy barrier, which gives rise to an experimental Na^+ conductivity of 5.0×10^{-2} mS cm^{-1}. In contrast, the 1D diffusion of HCF-Sm and HCF-La hinders macroscopic percolation due to lattice mismatching between polycrystalline and results in low experimental Na^+ conductivities of 1.1×10^{-4} and 5.5×10^{-5} mS cm^{-1} at RT (**Fig. S1d-f**), respectively. Based on the analysis, both types of Na-based halide materials currently have their limitations, leading to low apparent ionic conductivities. Therefore, due to the distinct metal-halogen polyhedral formation between HCF-Sm/La and LCF-Ta, a combination of the two shall likely form a heterogeneous structure rather than a solid solution, thus fully utilizing the fast 1D Na^+ diffusion in UCl_3-type HCFs and their capability of inducing amorphization.

The optimal composition of halide HSEs between HCF and LCF was investigated. The diffraction patterns of the heterostructures are shown in **Fig. 1f-g**. As the LCF-Ta content decreases, the diffraction peaks become weaker, leading to a noticeable increase in the dominance of the HCF-Sm/HCF-La diffraction peaks. The resulting HSEs exhibit enhanced ionic conductivities compared with the individual LCF-Ta and HCF-Sm/HCF-La samples (**Fig. 1h**). As illustrated in **Fig. 1i-j**, both in (1–*x*)[HCF-Sm]·*x*[LCF-Ta] and (1–*x*)[HCF-La]·*x*[LCF-Ta], the ionic conductivity is optimized within the range of $x = 0.35–0.5$. Notably, the composition 0.62[HCF-Sm]·0.38[LCF-Ta] demonstrates an exceptional ionic conductivity of 2.7 mS cm^{-1} at 25 °C, while 0.57[HCF-La]·0.43[LCF-Ta] exhibits a comparable ionic conductivity of 1.8

mS cm^{-1} at 25 °C. These values represent the highest conductivities achieved to date for halide SSCs (0.02-0.11 mS cm^{-1}). In addition, as proof of the generality of the halide HSE design, LCF-Ta was further replaced with Na_2ZrCl_6 (LCF-Zr) or Na_2HfCl_6 (LCF-Hf), respectively. The corresponding ionic conductivity also increased from the level of 0.01 mS cm^{-1} (pristine Na_2ZrCl_6 or Na_2HfCl_6) to the level of 0.1 mS cm^{-1} (heterostructures) as shown in **Fig. 1k**. The synchrotron-based X-ray diffraction (SXRD) observed similar sharp peaks from HCF-Sm/HCF-La and large bumps around $2\theta = 4$ ° ($\lambda = 0.3497$ Å) from LCF-Zr/LCF-Hf (**Fig. S2a-b**), confirming the formation of heterostructures.

To investigate the structural characteristics of HSEs, we conducted SXRD and PDF measurements on 0.62[HCF-Sm]·0.38[LCF-Ta] and 0.57[HCF-La]·0.43[LCF-Ta], as depicted in **Fig. 2a-b**. After heterogenized and synthesis of HSEs, the diffraction peaks relevant to LCF-Ta seem greatly quenched. Indeed, the crystalline LCF-Ta transforms into an amorphous state instead of forming a solid solution with HCF-Sm or HCF-La. The distribution of distances G(r) between pairs of atoms in 0.62[HCF-Sm]·0.38[LCF-Ta] and 0.57[HCF-La]·0.43[LCF-Ta] can be found in **Fig. 2c**. The peak at approximately 2.4 Å characterizes the Ta-Cl distance in octahedron of LCF-Ta, and the peak at ~2.8–2.9 Å characterizes the Sm/La-Cl distance in tricapped trigonal prisms of HCF-Sm/La. Both 0.62[HCF-Sm]·0.38[LCF-Ta] and 0.57[HCF-La]·0.43[LCF-Ta] present a mixed characteristic of $[TaCl_6]^-$ octahedron and $[MCl_9]^{6-}$ tricapped trigonal prisms (M = La, Sm), which confirms that 0.62[HCF-Sm]·0.38[LCF-Ta] and 0.57[HCF-La]·0.43[LCF-Ta] are a composite of crystalline HCF-Sm/HCF-La and amorphous LCF-Ta. Similarly, $[ZrCl_6]^{2-}$ or $[HfCl_6]^{2-}$ octahedrons have been identified in the PDF of HSEs using LCF-Zr or LCF-Hf (**Fig. S2c-d**). The "box-car fitting" was utilized to extract quantitative information about the length scale of local atomic order from the PDF analysis of complex materials.[42] Examination of the PDF through a box-car fitting method (box length of 6 Å, where the centroid of the refinement range is shifted to higher *r* in 1 Å steps) showed that fitted ratio of LCF-Ta in 0.62[HCF-Sm]·0.38[LCF-Ta] and 0.57[HCF-La]·0.43[LCF-Ta] changed as a function of fitting length scale. The ratio of LCF-Ta rapidly declines at around $r_{max} = 9$ Å and approaches *ca.* zero at $r_{max} = 18$ Å, which confirms the amorphization of LCF-Ta.

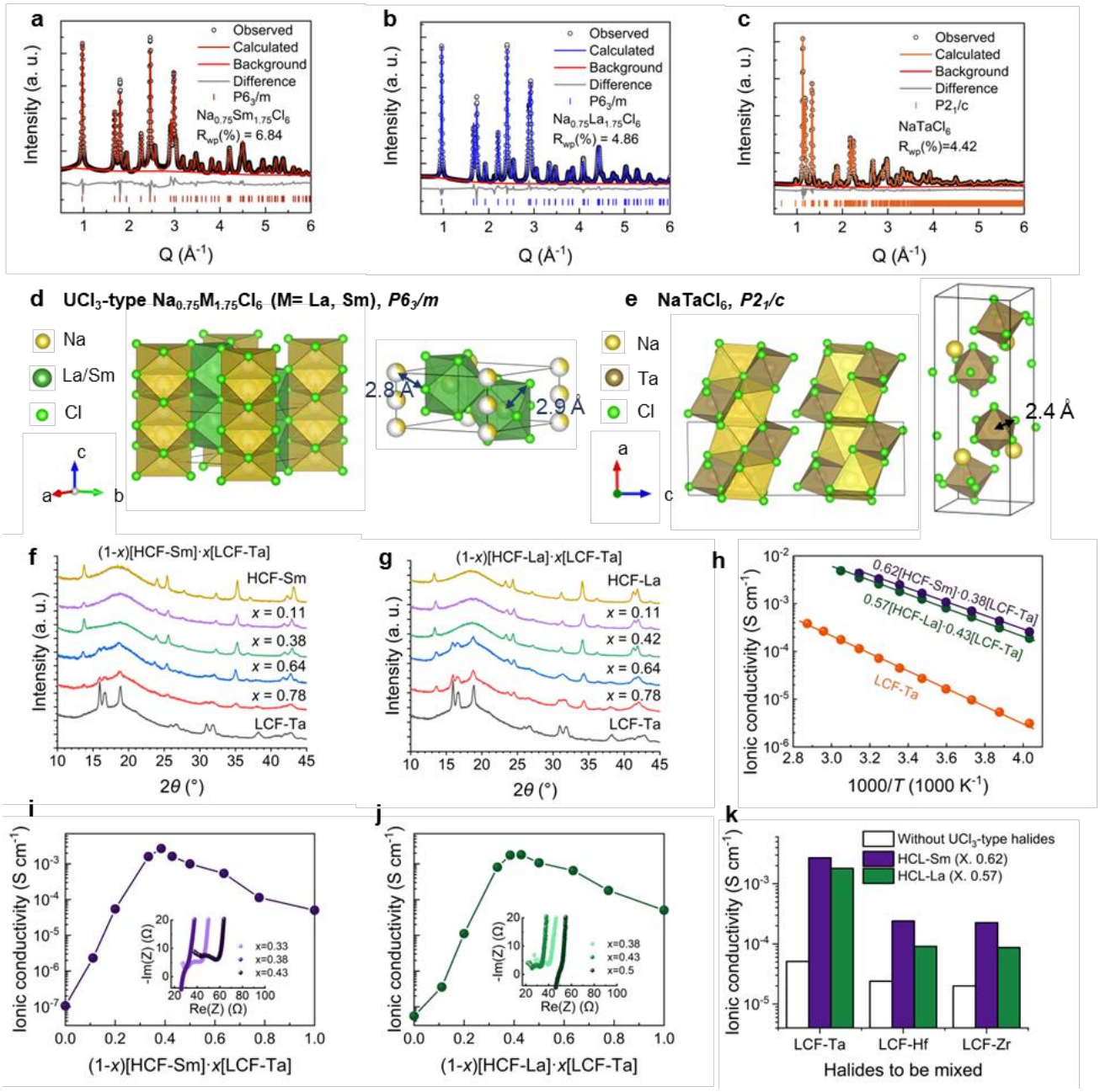

Figure 1 HCF-Sm/La, LCF-Ta, and their heterogeneous composite. Synchrotron-based X-ray diffraction patterns and the Rietveld refinements of (a) $Na_{0.75}Sm_{1.75}Cl_6$ (HCF-Sm), (b) $Na_{0.75}La_{1.75}Cl_6$ (HCF-La), and (c) $NaTaCl_6$ (LCF-Ta). (d) The crystal structure of UCl_3-type $Na_{0.75}M_{1.75}Cl_6$ (M = La, Sm). (e) The crystal structure of $NaTaCl_6$. (f-g) The X-ray diffraction patterns of HCF-La, HCF-Sm, LCF-Ta and their composites (1-*x*)[HCF-Sm]·*x*[LCF-Ta] and (1-*x*)[HCF-La]·*x*[LCF-Ta]. (h) Arrhenius plots of the LCF-Ta, 0.62[HCF-Sm]·0.38[LCF-Ta], and 0.57[HCF-La]·0.43[LCF-Ta]. The ionic conductivities of (i) (1-*x*)[HCF-Sm]·*x*[LCF-Ta] and (j) (1-*x*)[HCF-La]·*x*[LCF-Ta] at 25 °C. (k) The ionic conductivities of

HSEs based on 0.62[HCF-Sm]·0.38LCF and 0.57[HCF-La]·0.43LCF using different LCFs.

The crystalline-amorphous heterostructure of 0.62[HCF-Sm]·0.38[LCF-Ta] particles was further confirmed by HRTEM analysis. The HRTEM image of 0.62[HCF-Sm]·0.38[LCF-Ta] (**Fig. 2d-e**) clearly shows several grains that are spread throughout the particle and interconnected by the amorphous region. Combined XRD and the SEAD (**Fig. S3a**) results, the crystalline regions were identified as HCF-Sm, and its (020) and (011) planes were indicated in **Fig. 2d**. Moreover, the corresponding energy-dispersive X-ray spectroscopy (EDS) mapping on the whole particle (**Fig. S3b**) demonstrates a uniform distribution of Na and Cl elements but a slightly localized distribution of Sm and Ta elements, which further supports that the 0.62[HCF-Sm]·0.38[LCF-Ta] sample is a mixture rather than a solid solution.

To distinguish the Na^+ diffusion of different components, we studied the low-temperature electrochemical impedances of 0.62[HCF-Sm]·0.38[LCF-Ta], HCF-Sm, and LCF-Ta. The LCF-Ta presents a symmetric impedance semicircle (**Fig. S4a**) at -70 ℃, whereas both HCF-Sm (**Fig. S4b**, 5 ℃) and 0.62[HCF-Sm]·0.38[LCF-Ta] (**Fig. 2f**, -70 ℃) present an asymmetric impedance semicircle. By fitting the impedance result of 0.62 HCF-Sm·0.38 LCF-Ta, the origins of ionic conductivity were differentiated as the bulk-phase HCF-Sm, amorphous LCF-Ta, and interface/grain boundaries according to the capacitances from low to high, as depicted in **Fig. 2g**.[43] The ionic diffusions in these three regions exhibit a remarkable enhancement when compared to those observed in pristine HCF-Sm or LCF-Ta. Thus, the study of synergistic ion conduction among the crystalline region, the amorphous region, and the interface between crystalline and amorphous warrants thorough investigation.

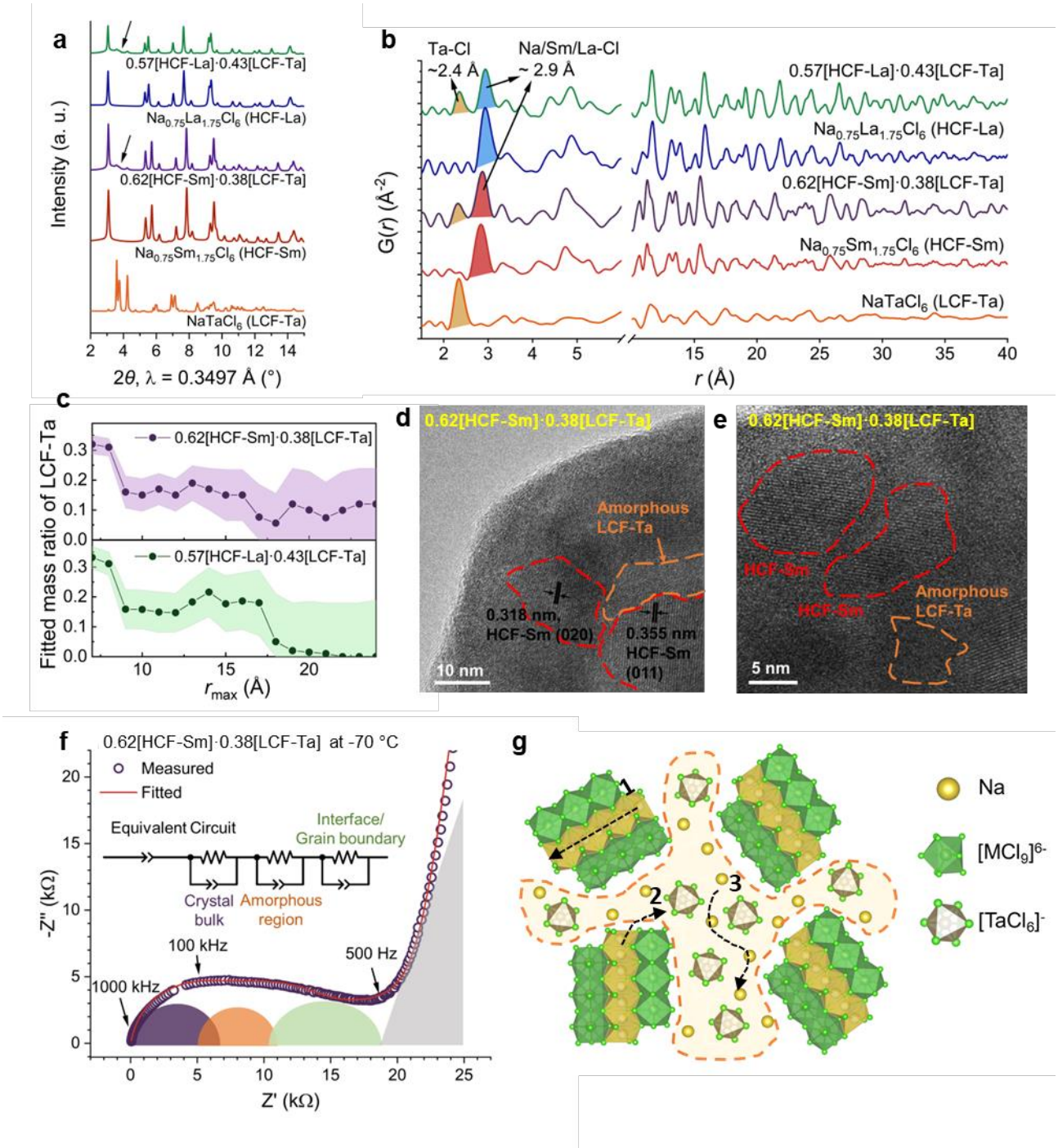

Figure 2 Crystalline-amorphous heterogeneous structures and enhanced ionic conductivities. (a) The high-resolution X-ray diffraction patterns and (b) pair distribution functions of LCF-Ta, HCF-La, HCF-Sm, 0.62[HCF-Sm]·0.38[LCF-Ta], and 0.57[HCF-La]·0.43[LCF-Ta]. (c) The fitted mass ratio of LCF-Ta in 0.62[HCF-Sm]·0.38[LCF-Ta], and 0.57[HCF-La]·0.43[LCF-Ta] verse r_{max} from the box-car fitting method. (d-e) HRTEM image taken from the particle edge of 0.62[HCF-Sm]·0.38[LCF-Ta]. (f) The

electrochemical impedance plot of 0.62[HCF-Sm]·0.38[LCF-Ta] at -70 ℃. (g) The schematic diagram of heterogeneous halide composites.

The synergistic effect enabled by heterogenization

To decipher the ion transport in the complex system of HSEs, we began by individually considering the impacts of the crystalline region, the amorphous region, and the interface. Previous studies have examined the space charge layer effect at interfaces[31,44-46] and the diffusion mechanism in UCl_3-type frameworks[40,41]. Here, we employ simulations to evaluate the influence of amorphous LCF-Ta on Na^+ diffusion. To generate the amorphous structure, we conduct thermal quenching of the crystalline LCF-Ta at temperatures of 1200 K and 2000 K and obtain two amorphous structures with increased disordering (**Fig. 3a-c**). While Ta-Cl remains local octahedral configurations in the amorphous structures, a notable change in Ta cation ordering is observed in amorphous LCF-Ta, leading to the diverse local environment of Na^+ sites (as illustrated in **Fig. 3d** and **Fig. S5**). The disordering of the $[TaCl_6]^-$ framework was further illustrated by the calculated radial distribution functions as shown in **Fig. 4a-b**, and the continuous symmetry measure (CSM) analysis suggests stronger distortion of the $[TaCl_6]^-$ octahedrons in amorphous LCF-Ta (**Fig. 4c**, 2000K-quenched > 1200K-quenched > Pristine), which is correlated with ionic conductivity as shown in **Fig. 3e**. According to the mechanism of ion diffusion in frustration as illustrated in Ref. 47,[47] the Na^+ hopping between these disordered sites has reduced barriers, thus enhancing the ionic conductivity as shown in AIMD simulations (**Fig. 3e**, 2000 K-quenched > 1200 K-quenched > Pristine).

Extended X-ray absorption fine structure (EXAFS) is a technique that enables the analysis of local structural information around a specific element absorber, making it an ideal tool for investigating the local coordination of specific elements in complex systems. The Fourier-transformed (FT) k^2-weighted $\chi(k)$ of Ta L_3-edge EXAFS spectra of LCF-Ta, 0.62[HCF-Sm]·0.38[LCF-Ta], and 0.57[HCF-La]·0.43[LCF-Ta] are present in **Fig. 4d**. The backscattering signals from the first shell of Ta atoms settle at R ~ 2.4 Å (after phase correction) in LCF-Ta, 0.62[HCF-Sm]·0.38[LCF-Ta], and 0.57[HCF-La]·0.43[LCF-Ta], consistent

with the Ta-Cl distance obtained from the PDF analysis. Similarly, the Sm L_3-edge EXAFS spectra of 0.62[HCF-Sm]·0.38[LCF-Ta] demonstrate only one characteristic peak located at R ~ 2.8 Å in **Fig. S6d**, which is identical to that of HCF-Sm and should be ascribed to the backscattering from Cl^- coordination in $[SmCl_9]^{6-}$ tricapped trigonal prisms. This excludes the probability that Ta and Sm are partially displacing each other in the mixture of LCF-Ta and HCF-Sm. Further, in the multiple-scattering region of **Fig. 4d and Fig. S7**, the focused hinge paths (Ta-Cl-Ta-Cl-Ta at R > 4 Å) are very sensitive to the bond angle of Cl-Ta-Cl as depicted in **Fig. 4e-f** (the closer to 180°, the stronger). After further differentiation of scattering signs in *k*-space (**Fig. 4g-i**), the peak intensity of *f1* at $k \sim 6$ $Å^{-1}$ and R ~ 4.2 Å can be viewed as a criterion of distortion of $[TaCl_6]^-$ octahedrons. Following the amorphization of LCF-Ta in the heterostructure, we observe a notable increase in the distortion of $[TaCl_6]^-$ octahedrons. This distortion causes a deviation of the central Ta atom, as evidenced by the decrease in the intensity of *f1* in the heterostructure (**Fig. 4i**) compared to pristine LCF-Ta (**Fig. 4h**). The distorting tendency strongly corroborates with our computational simulations, revealing notable alterations in the local environment of Ta within LCF-Ta.

Based on the analysis of the amorphous region, the interplay between the three regions in halide HSEs can be summarized as follows: the LCF-Ta transition into an amorphous state characterized by disordering $[TaCl_6]^-$ octahedrons when forming the heterogeneous interface with the UCl_3-type framework (i.e. HCFs); The disordering of $[TaCl_6]^-$ octahedrons leads to the diverse local environment of Na^+ sites with enhanced Na^+ ionic conductivity. These inter-grain amorphous regions then play a critical role in connecting different UCl_3-type frameworks, enabling long-range transmission within the grains and the amorphous region itself. The heterogeneous interface makes a substantial contribution to the overall ionic conductivity. However, comprehending and simulating this interface presents significant challenges, which will be the focus of our future research. Overall, the three regions synergistically enhanced the ionic conduction via the heterogenization of halide HSEs.

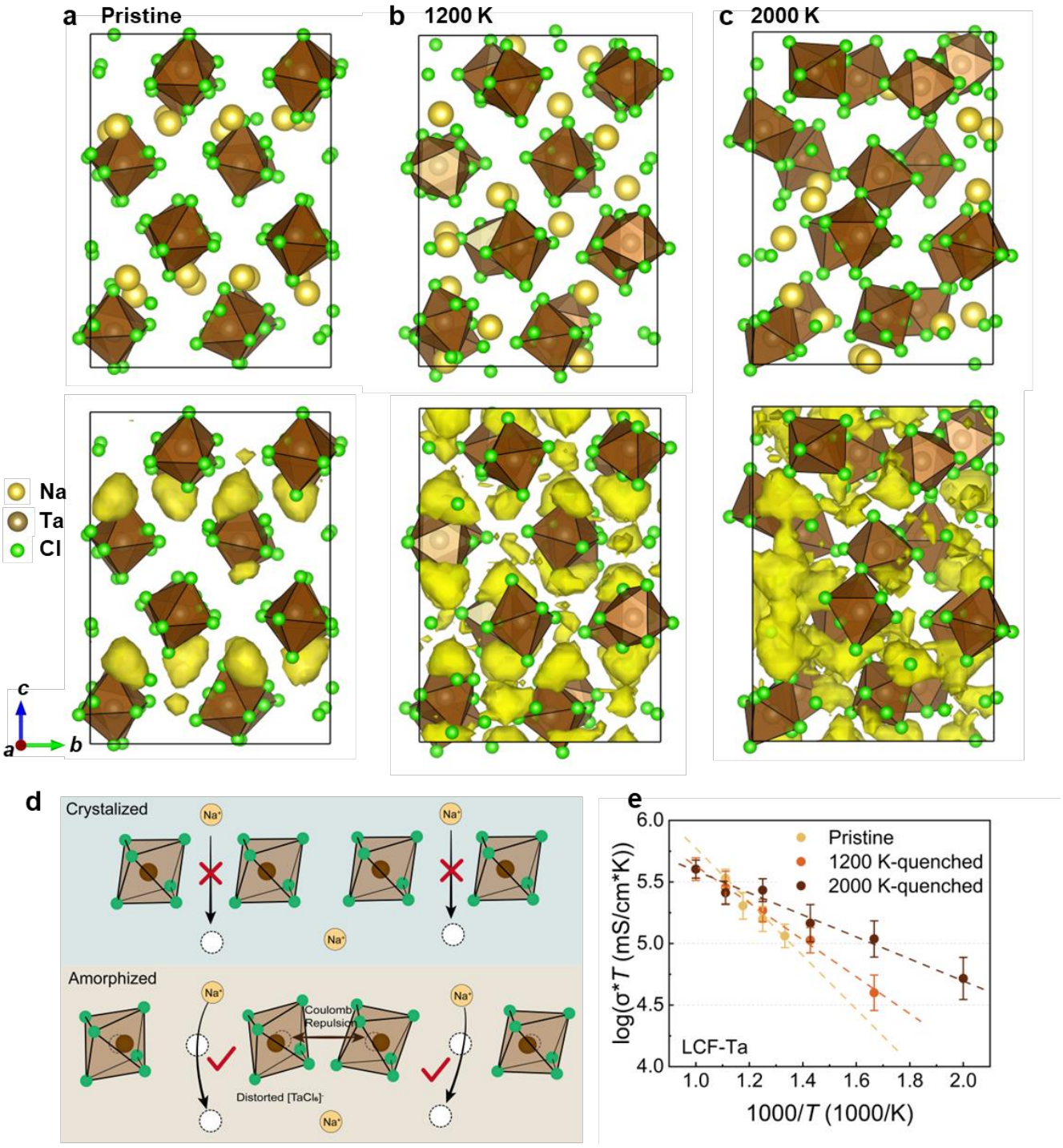

Figure 3 The effect of amorphization of LCF-Ta. Structures of (a) pristine LCF-Ta, (b) 1200 K-quenched LCF-Ta, and (c) 2000 K-quenched LCF-Ta. Below is the Na^+ probability density marked by yellow isosurfaces from AIMD simulations at 700 K. (d) Schematics of Na^+ diffusion in crystal versus amorphized LCF-Ta. (e) Arrhenius plot of Na^+ conductivity of crystalline LCF-Ta, 1200 K-quenched LCF-Ta, and 2000 K-quenched LCF-Ta.

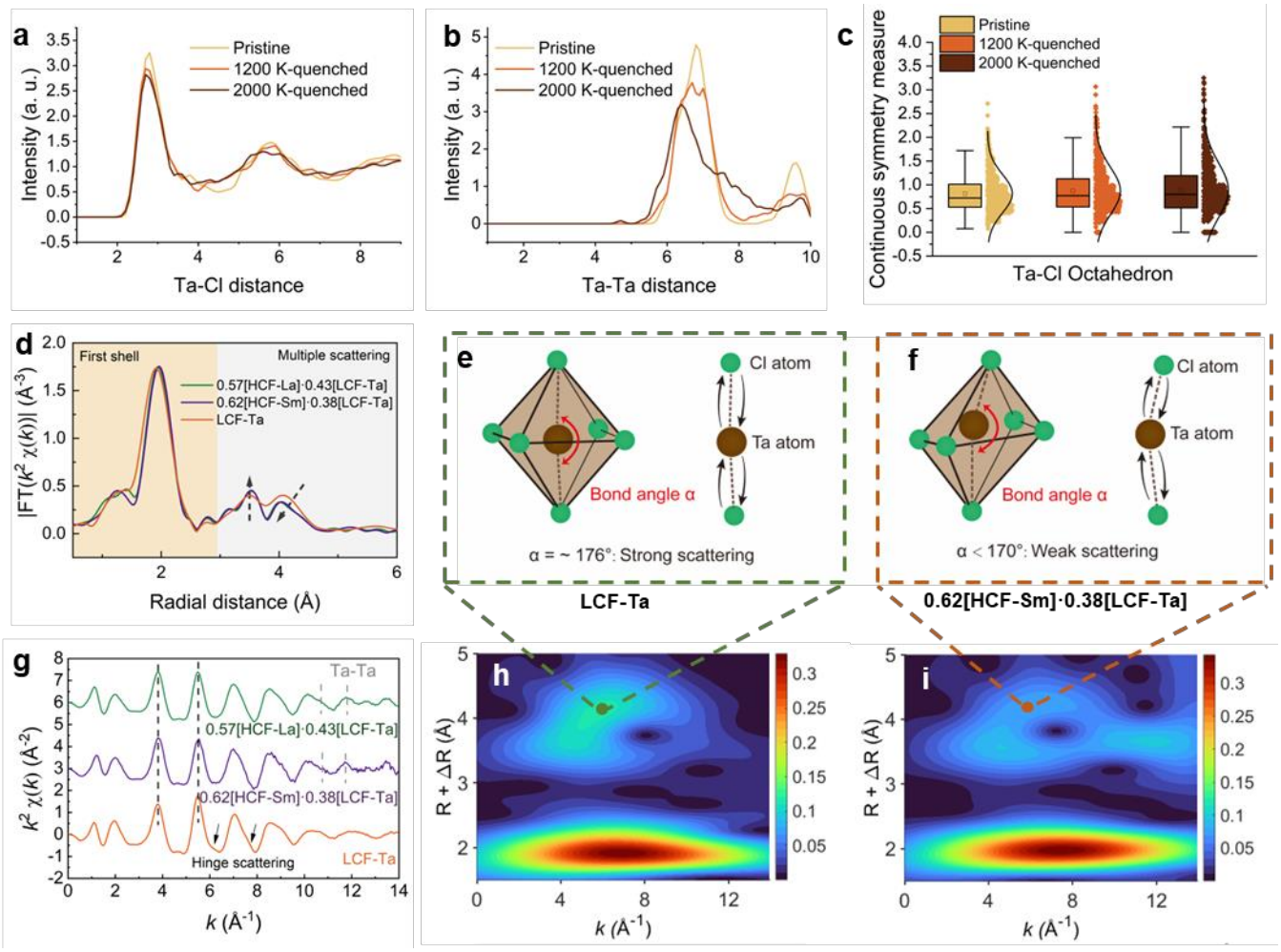

Figure 4 Local distortion in the amorphous LCF-Ta. Calculated radial distribution functions of (a) Ta-Cl distance and (b) Ta-Ta distance of LCF-Ta. (c) Continuous symmetry measure of Ta-Cl Octahedra in LCF-Ta. For each box, the centerline marks the median of the data set, the center square marks the mean of the data set, the outer edges mark the first and third quartiles, and the endpoints are either the extrema values or 1.5 times the interquartile range, whichever is smaller. Data are marked individually as diamonds. All the configurations are sampled at constant 2 ps intervals from the snapshots in AIMD simulation at 600K. (d) Fourier transform of the Ta L_3-edge EXAFS in R-space, with a k^2-weighing, of LCF-Ta, 0.62[HCF-Sm]·0.38[LCF-Ta], and 0.57[HCF-La]·0.43[LCF-Ta]. (e-f) The schematic of the relationship between bond angle and the intensity of multiple scattering. (g) The Ta L_3-edge EXAFS region in k-space of LCF-Ta, 0.62[HCF-Sm]·0.38[LCF-Ta], and 0.57[HCF-La]·0.43[LCF-Ta]. Wavelet transform of the k^2-weighted EXAFS data of (h) LCF-Ta and (i) 0.62[HCF-Sm]·0.38[LCF-Ta].

The SSSB performance using halide HSEs

In addition to their excellent ionic conductivity compared to other halide electrolytes, halide HSEs also possess favorable properties such as deformability and exceptional high-voltage stability. The deformability of solid electrolytes can be directly assessed by examining the relative porosity of cold-pressed pellets under a specific pressure. We pressed the electrolyte powders into a pellet under *ca.* 400 MPa. The cross-sectional morphologies of these pellets were examined by scanning electron microscopy (SEM). The pellets of 0.62[HCF-Sm]·0.38[LCF-Ta] and 0.57[HCF-La]·0.43[LCF-Ta] are much denser than the typical sulfide SSC of Na_3PS_4, as depicted in **Fig. S8a-c**. Pores and voids are clearly observed in high-magnification images of Na_3PS_4 but absent in halide HSEs (**Fig. S8d-e**).

The thermodynamic electrochemical windows (vs Na/Na^+) of HCF-Sm, HCF-La, LCF-Ta, and Na_3PS_4 were calculated using the grand potential phase diagram approach (**Fig. 5a**). The stable electrochemical windows were determined as 0.64–4.25 V for HCF-Sm and 0.41–3.76 V for HCF-La, respectively. LCF-Ta has a similar oxidation limit of 3.91 V but a high reduction limit of 2.15 V due to the reduction of Ta^{5+}. Overall, halide SSCs generally demonstrate higher oxidation limits than sulfides, such as Na_3PS_4 (1.21 - 2.12 V). The experimental electrochemical windows of 0.62[HCF-Sm]·0.38[LCF-Ta] and 0.57[HCF-La]·0.43[LCF-Ta] are measured using linear sweep voltammetry (LSV) analyses. Matching with theoretical prediction results, 0.62[HCF-Sm]·0.38[LCF-Ta] has a higher oxidation limit than that of 0.57[HCF-La]·0.43[LCF-Ta] (**Fig. S9**).

The chemical/electrochemical stabilities between LCF-Ta and other SSCs and various cathode materials were further evaluated by computation[48,49]. **Fig. 5b** and **Table S5-8** depict the reaction energy and decomposition products between SSCs and cathode materials including NMNFO, $NaCrO_2$, and $Na_3V_2(PO_4)_3$. The de-sodiation of these three cathode materials notably results in instability in contact with Na_3PS_4. Conversely, halide SSCs show greater stability as the Na content decreases. As the options of metal elements for halide HSEs are versatile (e.g., Sm/La and Ta/Zr/Hf) without significantly

compromising the high ionic conductivity of the electrolyte, the electrochemical window of halide HSEs and composition of cathode electrolyte interface (CEI) are tunable.

As a proof of concept, the compatibility between different halide HSEs and cathode active materials was studied in SSSBs. A Na_3PS_4 interlayer was inserted between the HSEs and the $Na_{15}Sn_4$ alloy anode. NMNFO was selected as a representative cathode material due to its appropriate operating voltage up to 4 V. **Fig. 5c** presents the initial charge-discharge curves of NMNFO-based SSSBs using different electrolytes at 0.1 C (1 C = 120 mAh g^{-1}). As a control experiment, the cell using only Na_3PS_4 as the electrolyte showed little discharge capacity after being charged to 4 V. In sharp contrast, the cells using either 0.62[HCF-Sm]·0.38[LCF-Ta] or 0.57[HCF-La]·0.43[LCF-Ta] exhibited a reversible charge-discharge process. The interfacial reaction between different electrolytes and NMNFO was investigated by X-ray photoelectron spectroscopy (XPS). As indicated in **Fig. S10a-b** for the cell using Na_3PS_4, both S *2p* and P *2p* XPS spectra exhibited strong signals from P_2S_5 and bridging sulfur (P-$[S]_n$-P), indicating a severe decomposition of Na_3PS_4 at 4 V, and this result is consistent with previous reports on electrodes using Na_3PS_4.[27] As for the cells using halide HSEs, marginal changes of Sm *3d*, La *3d*, Ta *4f*, and Cl *2p* spectra were observed after being charged to 4 V (**Fig. S10c-h**), confirming the exceptional cationic stability of 0.62[HCF-Sm]·0.38[LCF-Ta] and 0.57[HCF-La]·0.43[LCF-Ta] compared to that of Na_3PS_4. As we have exhibited above, the electrochemical performance of HSEs is far superior to that of Na_3PS_4 when charging the cell to 4 V vs Na/Na^+.

The rate and cycle performance of cells using 0.62[HCF-Sm]·0.38[LCF-Ta] or 0.57[HCF-La]·0.43[LCF-Ta] are comparable, as depicted in **Fig. 6d-g**. Specifically, the 0.57[HCF-La]·0.43[LCF-Ta] cell showed capacity retention of 91.0 % after 100 cycles at 0.2 C, which is slightly higher than the 0.62[HCF-Sm]·0.38[LCF-Ta] cell (88.3 %). To be noted, the observed performance at high rates is mainly limited by the poor ionic conductivity of the interlayer Na_3PS_4 (~0.1 mS cm^{-1}). While the ionic conductivities of 0.62[HCF-Sm]·0.38[LCF-Ta] and 0.57[HCF-La]·0.43[LCF-Ta] are comparable, the discharge capacity and Coulombic efficiency (CE) in the initial cycle is higher when using 0.62[HCF-Sm]·0.38[LCF-Ta] than

using 0.57[HCF-La]·0.43[LCF-Ta] (~117.9 mAh g^{-1} vs. ~95.1 mAh g^{-1}; 96.1 % vs. 85.8 %). This can be attributed to the higher oxidation limit of 0.62[HCF-Sm]·0.38[LCF-Ta] due to the use of HCF-Sm instead of HCF-La. Recent research has shown the critical role of metal elements in halide electrolytes in determining the high-voltage stability of the battery.[50] Within HSEs, the choice of components also affects the performance of the battery as the 0.62[HCF-Sm]·0.38[LCF-Ta] cell delivered higher discharge capacity whereas the 0.57[HCF-La]·0.43[LCF-Ta] cell exhibited better cycle performance.

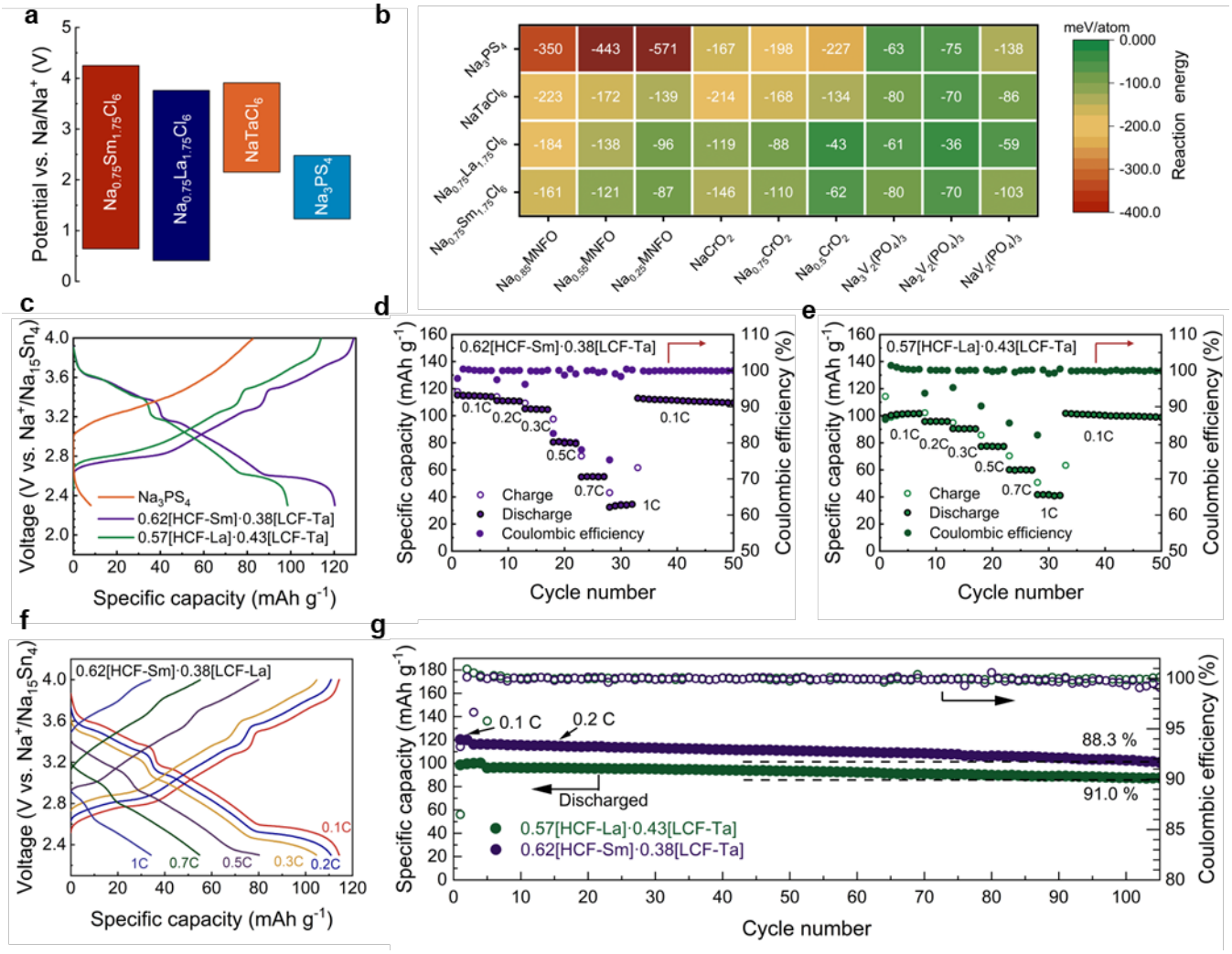

Figure 5 Electrochemical stability and battery performance. (a) The calculated stable electrochemical window of different solid electrolytes. (b) Thermodynamic calculation of decomposition energies between solid electrolytes and cathode materials at sodiated and de-sodiated states. (c) The 1st charge/discharge profile of cells in which 0.62[HCF-Sm]·0.38[LCF-Ta], 0.57[HCF-La]·0.43[LCF-Ta], or Na_3PS_4 is used as

catholyte at room temperature and 0.1 C (1C = 120 mAh g^{-1}). (d-e) the rate performance of cells using 0.62[HCF-Sm]·0.38[LCF-Ta] and 0.57[HCF-La]·0.43[LCF-Ta] as catholyte at room temperature. (f) the charge/discharge curves of the cell in (e) at various current densities. (g) The long cycle performance of cycled between 2.3-4 V vs. Na^+/Na at 0.2 C at 25 ℃.

Conclusion

In summary, our findings lead to a novel class of halide HSEs by utilizing the synergistic effect between high- and low-coordination halide frameworks, demonstrating an impressive combination of high ionic conductivity, excellent high-voltage stability, and deformability. The optimized 0.62[HCF-Sm]·0.38[LCF-Ta] and 0.57[HCF-La]·0.43[LCF-Ta] HSEs exhibited remarkable Na-ion conductivity of 2.7 mS cm^{-1} and 1.8 mS cm^{-1}, which are among the highest value reported so far for halide SSCs. The diffusion mechanism in this class of halide HSEs was studied, revealing distinct contributions from crystalline bulk, amorphous region, and interface. In particular, the effect of amorphized components in HSEs was studied. The amorphization process significantly increases the ionic conductivity of target components and assists to establish connections between discrete UCl_3-type framework particles, thereby enabling fast long-range Na-ion conduction across the macroscopic HSEs. With good deformability and high-voltage stability of HSEs, direct integration with NMNFO cathode can be achieved by simple cold-pressing to demonstrate a stable cathode/catholyte interface and a capacity retention of 91.0 % after 100 cycles at 0.2 C for SSSBs. In addition, a theoretical study of interfacial reactions between SSCs and cathode materials revealed different interfacial products upon the choice of SSCs or cathode materials. The component in HSEs is versatile, allowing for a tunable CEI design for different cathode materials. Owing to the comprehensive advantages, the heterogeneous halide composite SSC is an ideal choice for achieving high-performance SSSBs.

Acknowledgments

The authors thank the support from the Natural Sciences and Engineering Research Council of Canada (NSERC), the Canada Research Chair Program (CRC), the Canada Foundation for Innovation (CFI), and Western University. The synchrotron-related characterizations were completed at the HXMA, SXRMB, and BXDS beamline in Canadian Light Source (CLS), which is supported by the Canada Foundation for Innovation (CFI), the Natural Sciences and Engineering Research Council (NSERC), the National Research Council (NRC), the Canadian Institutes of Health Research (CIHR), the Government of Saskatchewan, and the University of Saskatchewan. M. Gu wants to acknowledge the support from Guangdong Fundamental Research Association with the project no. 2022B1515120013, National Natural Science Foundation of China (52273225), Guangdong scientific program with contract no. 2019QN01L057. Y. Mo acknowledge the funding support from National Science Foundation Award# 2118838 and the computational facilities from the University of Maryland supercomputing resources.

Author contributions

J. Fu and S. Wang conceived the project. J. Fu performed the electrolyte synthesis and characterization. S. Wang performed the computational simulations. X. Ling helped with the fabrication of SSSBs. D. Wu and M. Gu. conducted TEM measurements and analyses. The other authors partially contributed to the experiment design and data analysis. J. Fu, S. Wang, and J. Luo formally analyzed all data and wrote the manuscript. M. Gu, T. K. Sham, Y. Mo, and X. Sun supervised the project. All the authors participated in the reviewing and editing of the manuscript.

EXPERIMENTAL PROCEDURES

DFT Calculation

We performed all density functional theory (DFT) calculations using Vienna Ab initio Simulation package (VASP)[51] within the projector augmented-wave (PAW) approach[52] and Perdew–Burke–Ernzerhof (PBE)

generalized-gradient approximation (GGA) functional[53]. The convergence parameters in static DFT calculations were consistent with the Materials Project[54].

Generation of Amorphous structures

The supercell models of crystal $NaTaCl_6$ (a total of 128 atoms) were heated from 100 K to target temperature (1200 K and 2000 K) at a constant rate within a period of 2 ps and then equilibrated for 20 ps. Finally, the configurations were quenched to 100K at a constant rate within a period of 2 ps. In all simulations, non-spin-polarized mode, a time step of 2 fs, and NVT ensemble using a Nose´-Hoover thermostat[55] were used.

ab initio molecular dynamics (AIMD) Simulations

To investigate ionic diffusion, we performed AIMD simulations on the supercell models of HCF-SM (a total of 68 atoms), HCF-LA (a total of 68 atoms), and LCF-TA (a total of 128 atoms). Non-spin-polarized mode and a Γ-centered k-point were used. A time step of 2 fs and NVT ensemble using a Nose´-Hoover thermostat[55] was used in all simulations. The structures were heated from 100 K to the targeted temperature (400-1000 K) at a constant rate during a period of 2 ps. The D was calculated as the mean square displacement (MSD) over the time interval Δt:

$$D = \frac{1}{2Nd\Delta t} \sum_{i=1}^{N} \langle [\mathbf{r}_i(t + \Delta t) - \mathbf{r}_i(t)]^2 \rangle_t$$

The ionic conductivity was calculated according to the Nernst-Einstein relationship:

$$\sigma = \frac{nq^2}{k_B T} D$$

where n is the mobile ions volume density and q is the ionic charge. The activation energy and ionic conductivity at desired temperature were extrapolated according to the Arrhenius relation:

$$\sigma T = \sigma_0 \exp\left(\frac{-E_a}{k_B T}\right)$$

where E_a is activation energy, σ_0 is the pre-exponential factor. The statistical deviation of the diffusivity was evaluated using the scheme established in our previous work[56], then the simulations lasted 40 to 300 ps until the diffusivity converged within a relative standard deviation of 20-40%. The Li-ion probability density was calculated as the time fraction of Li-ions at each spatial location in the crystal structures during the AIMD simulations. The demonstration of crystal structure was performed by VESTA software[57].

Thermodynamic calculations of Interface stabilities

To evaluate the interfacial stability between solid electrolytes (SE) and common cathode materials, the interface pseudo-binary reaction energy was calculated as:

$$\Delta E_D(\text{SE, cathode}, x) = E_{eq}(C_{interface}(C_{SE}, C_{cathode}, x)) - E_{interface}(\text{SE, cathode}, x)$$

where C_{SE} and $C_{cathode}$ are the compositions of solid electrolyte (SE) and cathode materials, normalized to one atom per formula. The x is the molar fraction of the SE. The energies of materials were obtained from MP database. More details can be found in previous studies[58-60].

Thermodynamic calculations of Electrochemical window

The electrochemical window was evaluated using the method in our previous studies[58,61]. A grand potential phase diagram was used to identify the phase equilibria of a given phase in equilibrium with Na reservoir at chemical potential μ_{Na} referenced to Na metal. The stable electrochemical window of the phase was estimated as the range of μ_{Na}, where the phase is neither oxidized nor reduced.

Synthesis methods

All preparation processes and sample treatments were carried out in an Ar-filled glovebox (O_2 < 1 ppm, H_2O < 1 ppm). The UCl_3-type halides HCF-Sm/HCF-La and ternary halides $NaTaCl_6$, Na_2ZrCl_6, and Na_2HfCl_6 were synthesized by ball-milling the starting materials of NaCl (Sigma Aldrich, 99.9 % purity),

$SmCl_3$ (Sigma Aldrich, 99.9 % purity) and $LaCl_3$ (Sigma Aldrich, 99.8 % purity), $TaCl_5$ (Sigma Aldrich, 99.99 % purity), $ZrCl_4$ (Sigma Aldrich, 99.9 % purity), and $HfCl_4$ (Sigma Aldrich, 99.9 % purity) at the stated stoichiometric ratio. For ball-milling synthesis, the mixture of precursors was sealed in a zirconia jar (100 mL) under vacuum and ball-milled at 500 rpm for 60 cycles. Each cycle included 10-min milling and 5-min resting. The heterogeneous composite was synthesized by ball-milling as-prepared HCF-Sm/HCF-La and $NaTaCl_6$/Na_2ZrCl_6/Na_2HfCl_6 at 500 rpm for another 20 cycles.

Characterization

Lab-based X-ray diffraction (XRD) measurements were performed on Bruker AXS D8 Advance with Cu Kα radiation (λ = 1.5406 Å). Kapton tape was used to cover the sample holder to prevent air exposure. Scanning electron microscope (SEM) images and element mappings were obtained by using a Hitachi S-4800 field-emission scanning electron microscope (FE-SEM, acceleration voltage 5 kV) equipped with energy dispersive spectroscopy (EDS). High-resolution transmission electron microscopy (HRTEM) images, energy dispersive spectrometry (EDS) mapping, and selected area electron diffraction (SAED) patterns of the studied samples were performed by a Cs-corrected Titan Themis 80–300 TEM, operated at 300 kV, fitted with a Bruker Quantax Super-X EDS detector. The sample powder was directly dispersed on a Cu grid without the assistance of solvent. Elemental maps were acquired at a beam current of 200 pA and an acquisition time of 10–15 min. A standard-based quantification method (Linemarker TEM) was used for the elemental quantification of the acquired elemental maps.

Synchrotron-based powder diffraction and pair distribution function were collected using the Brockhouse High Energy Wiggler beamline at the Canadian Light Source (CLS) with a wavelength of 0.3497 Å. The samples were loaded into 0.8 mm inner diameter polyimide capillaries and sealed with epoxy in an Ar-filled glove box. The X-ray diffraction Rietveld refinement and pair distributed function fittings were conducted by GSAS-2 and PDFgui software.[62,63] X-ray absorption spectra (XAS) were collected from the Hard X-ray Micro-Analysis (HXMA) and Soft X-ray Micro characterization (SXRMB) beamlines of CLS,

the samples were mixed with BN and pressed into pellets to achieve an absorption length of 1. Samples for Cl K-edge were spread on carbon tape and measured within a vacuum chamber. All XAS data were analyzed with the Athena software, and the EXAFS data were processed using the Artemis program.[64]

Electrochemical characterizations

The temperature-dependent ionic conductivities of prepared SSEs were obtained via the EIS measurements of model cells on a multichannel potentiostat 3/Z (German VMP3). The applied frequency range was 1 Hz to 7 MHz and the voltage amplitude was 20 mV. The test cell was fabricated by pressing electrolytes into a pellet ((~400 MPa, 120 mg samples, diameter of 1 cm, thickness ~0.5-0.6 mm). About 5 mg of acetylene black carbon was then spread onto both sides of the pellet and pressed with ~150 MPa.

The model SSSB was assembled by using the NMNFO as the cathode, Na-Sn (15:4) as the negative electrode, and halide HSEs and/or Na_3PS_4 as the separator (see diagram of battery architecture in Fig. S11). 100 mg of the electrolyte powder to be tested was pressed at ~200 MPa to form an SSE layer (1 cm diameter). The cathode composite (NMNFO: SSC: carbon black (CB) = 60:40:2) was uniformly spread onto the surface of one side of the electrolyte layer and pressed with ~400 MPa for one minute. Then about 7 mg of the cathode composite was placed on one side of the SSC pellet and pressed at the same pressure, and on the opposite side of SSC, the Na_3PS_4 and an excess of Na-Sn alloy (60 mg) were pressed in order. Galvanostatic charge-discharge for SSSB was conducted on the LAND battery test system at RT. The LSV measurement used the same configuration except that the cathode composite was replaced by the mixed powder of the SSC and CB in a weight ratio of 9:1 using a mortar and a pestle. The scan ranges from the open-circuit voltage (OCV) to 6 V (vs Na/Na^+, positive scan) or OCV to 0 V (vs Na/Na^+, negative scan), respectively. The scan rate was 0.1 mV s^{-1}.

Competing interests

The authors declare that they have no competing interests.

Data and materials availability

Data is available upon reasonable request to the authors.

Supporting Information

Supporting figures and tables.

References:

1 Yang, H.-L. *et al.* Progress and Challenges for All-Solid-State Sodium Batteries. *Advanced Energy and Sustainability Research* **2**, doi:10.1002/aesr.202000057 (2021).

2 Vaalma, C., Buchholz, D., Weil, M. & Passerini, S. A cost and resource analysis of sodium-ion batteries. *Nat. Rev. Mater.* **3**, 1-11 (2018).

3 Hwang, J.-Y., Myung, S.-T. & Sun, Y.-K. Sodium-ion batteries: present and future. *Chem. Soc. Rev.* **46**, 3529-3614 (2017).

4 Sun, Y.-K. Promising All-Solid-State Batteries for Future Electric Vehicles. *ACS Energy Lett.* **5**, 3221-3223, doi:10.1021/acsenergylett.0c01977 (2020).

5 Abakumov, A. M., Fedotov, S. S., Antipov, E. V. & Tarascon, J. M. Solid state chemistry for developing better metal-ion batteries. *Nat. Commun.* **11**, 4976, doi:10.1038/s41467-020-18736-7 (2020).

6 Zhao, N. *et al.* Solid Garnet Batteries. *Joule*, doi:10.1016/j.joule.2019.03.019 (2019).

7 Yao, Y.-F. Y. & Kummer, J. Ion exchange properties of and rates of ionic diffusion in beta-alumina. *J. inorg. nucl. chem.* **29**, 2453-2475 (1967).

8 Goodenough, J. B., Hong, H.-P. & Kafalas, J. Fast Na^+-ion transport in skeleton structures. *Mater. Res. Bull.* **11**, 203-220 (1976).

9 Gigante, A. *et al.* Direct Solution-Based Synthesis of Na_4 $(B_{12}H_{12})(B_{10}H_{10})$ Solid Electrolyte. *ChemSusChem* **12**, 4832-4837 (2019).

10 Hayashi, A., Noi, K., Sakuda, A. & Tatsumisago, M. Superionic glass-ceramic electrolytes for room-temperature rechargeable sodium batteries. *Nat. Commun.* **3**, 856, doi:10.1038/ncomms1843 (2012).

11 Takeuchi, S., Suzuki, K., Hirayama, M. & Kanno, R. Sodium superionic conduction in tetragonal Na_3PS_4. *J. Solid State Chem.* **265**, 353-358, doi:10.1016/j.jssc.2018.06.023 (2018).

12 Feng, X. *et al.* Studies of Functional Defects for Fast Na-Ion Conduction in $Na_{3-y}PS_{4-x}Cl_x$ with a Combined Experimental and Computational Approach. *Adv. Funct. Mater.* **29**,

doi:10.1002/adfm.201807951 (2019).

13 Chu, I. H. *et al.* Room-Temperature All-solid-state Rechargeable Sodium-ion Batteries with a Cl-doped Na_3PS_4 Superionic Conductor. *Sci. Rep.* **6**, 33733, doi:10.1038/srep33733 (2016).

14 Hayashi, A. *et al.* A sodium-ion sulfide solid electrolyte with unprecedented conductivity at room temperature. *Nat. Commun.* **10**, 5266, doi:10.1038/s41467-019-13178-2 (2019).

15 Banerjee, A. *et al.* Na3SbS4: a solution processable sodium superionic conductor for all-solid-state sodium-ion batteries. *Angew. Chem., Int. Ed. Engl.* **128**, 9786-9790 (2016).

16 Bo, S.-H., Wang, Y., Kim, J. C., Richards, W. D. & Ceder, G. Computational and Experimental Investigations of Na-Ion Conduction in Cubic Na_3PSe_4. *Chem. Mater.* **28**, 252-258, doi:10.1021/acs.chemmater.5b04013 (2015).

17 Krauskopf, T., Pompe, C., Kraft, M. A. & Zeier, W. G. Influence of Lattice Dynamics on Na+Transport in the Solid Electrolyte $Na_3PS_{4-x}Se_x$. *Chem. Mater.* **29**, 8859-8869, doi:10.1021/acs.chemmater.7b03474 (2017).

18 Li, X. *et al.* Water-Mediated Synthesis of a Superionic Halide Solid Electrolyte. *Angew. Chem., Int. Ed. Engl.* **58**, 16427-16432, doi:10.1002/anie.201909805 (2019).

19 Li, X. *et al.* Air-stable Li_3InCl_6 electrolyte with high voltage compatibility for all-solid-state batteries. *Energy Environ. Sci.* **12**, 2665-2671, doi:10.1039/c9ee02311a (2019).

20 Zhou, L. *et al.* A new halospinel superionic conductor for high-voltage all solid state lithium batteries. *Energy Environ. Sci.* **13**, 2056-2063, doi:10.1039/d0ee01017k (2020).

21 Liang, J. *et al.* Site-Occupation-Tuned Superionic Li_xScCl_{3+x}Halide Solid Electrolytes for All-Solid-State Batteries. *J. Am. Chem. Soc.* **142**, 7012-7022, doi:10.1021/jacs.0c00134 (2020).

22 Wang, K. *et al.* A cost-effective and humidity-tolerant chloride solid electrolyte for lithium batteries. *Nat. Commun.* **12**, 4410, doi:10.1038/s41467-021-24697-2 (2021).

23 Kwak, H. *et al.* New Cost-Effective Halide Solid Electrolytes for All-Solid-State Batteries: Mechanochemically Prepared Fe^{3+}-Substituted Li_2ZrCl_6. *Adv. Energy Mater.* **11**, 2003190, doi:10.1002/aenm.202003190 (2021).

24 Asano, T. *et al.* Solid Halide Electrolytes with High Lithium-Ion Conductivity for Application in 4 V Class Bulk-Type All-Solid-State Batteries. *Adv. Mater.* **30**, e1803075, doi:10.1002/adma.201803075 (2018).

25 Schlem, R. *et al.* Mechanochemical Synthesis: A Tool to Tune Cation Site Disorder and Ionic Transport Properties of Li_3MCl_6 (M = Y, Er) Superionic Conductors. *Adv. Energy Mater.* **10**, 1903719, doi:10.1002/aenm.201903719 (2019).

26 Fu, J. *et al.* Superionic Conducting Halide Frameworks Enabled by Interface-Bonded Halides. *J.*

Am. Chem. Soc. **145**, 2183–2194 (2022).

27 Kwak, H. *et al.* Na_2ZrCl_6 enabling highly stable 3 V all-solid-state Na-ion batteries. *Energy Storage Mater.* **37**, 47-54, doi:10.1016/j.ensm.2021.01.026 (2021).

28 Schlem, R., Banik, A., Eckardt, M., Zobel, M. & Zeier, W. G. $Na_{3-x}Er_{1-x}Zr_xCl_6$—A Halide-Based Fast Sodium-Ion Conductor with Vacancy-Driven Ionic Transport. *ACS Appl. Energy Mater.* **3**, 10164-10173, doi:10.1021/acsaem.0c01870 (2020).

29 Wu, E. A. *et al.* A stable cathode-solid electrolyte composite for high-voltage, long-cycle-life solid-state sodium-ion batteries. *Nat. Commun.* **12**, 1256, doi:10.1038/s41467-021-21488-7 (2021).

30 Phillip Ridley *et al.* Glass-Ceramic Sodium-Deficient Chlorides with High Sodium-ion Conductivity. *ChemRxiv. Cambridge: Cambridge Open Engage*, doi:10.26434/chemrxiv-2022-x7llq (2022).

31 Zou, Z. *et al.* Mobile Ions in Composite Solids. *Chem. Rev.*, doi:10.1021/acs.chemrev.9b00760 (2020).

32 Kwak, H. *et al.* Boosting the interfacial superionic conduction of halide solid electrolytes for all-solid-state batteries. *Nat. Commun.* **14**, 2459, doi:10.1038/s41467-023-38037-z (2023).

33 Liang, C. Conduction characteristics of the lithium iodide-aluminum oxide solid electrolytes. *J. Electrochem. Soc.* **120**, 1289 (1973).

34 Patel, S. V. *et al.* Interrupted anion-network enhanced Li^+-ion conduction in $Li_{3+y}PO_4I_y$. *Energy Storage Mater.* **51**, 88-96, doi:10.1016/j.ensm.2022.06.026 (2022).

35 Tatsumisago, M., Torata, N., Saito, T. & Minami, T. Microstructure of superionic glassy composites with stabilized α-AgI. *J. Non-Cryst.* **196**, 193-198 (1996).

36 Mercier, R., Malugani, J.-P., Fahys, B. & Robert, G. Superionic conduction in Li_2S-P_2S_5-LiI-glasses. *Solid State Ion.* **5**, 663-666 (1981).

37 Choi, Y. S., Lee, Y.-S., Oh, K. H. & Cho, Y. W. Interface-enhanced Li ion conduction in a $LiBH_4$–SiO_2 solid electrolyte. *Phys. Chem. Chem. Phys.* **18**, 22540-22547 (2016).

38 Tambelli, C. *et al.* Characterisation of PEO–Al_2O_3 composite polymer electrolytes. *Electrochim. Acta* **47**, 1677-1682 (2002).

39 Zheng, J., Tang, M. & Hu, Y. Y. Lithium ion pathway within Li7La3Zr2O12-polyethylene oxide composite electrolytes. *Angew. Chem., Int. Ed. Engl.* **55**, 12538-12542 (2016).

40 Fu, J. *et al.* Superionic Conducting Halide Frameworks Enabled by Interface-Bonded Halides. *J. Am. Chem. Soc.* **145**, 2183-2194, doi:10.1021/jacs.2c09446 (2023).

41 Yin, Y. C. *et al.* A $LaCl_3$-based lithium superionic conductor compatible with lithium metal. *Nature* **616**, 77-83, doi:10.1038/s41586-023-05899-8 (2023).

42 Qiu, X., Proffen, T., Mitchell, J. & Billinge, S. Orbital correlations in the pseudocubic O and rhombohedral R phases of $LaMnO_3$. *Phys. Rev. Lett.* **94**, 177203 (2005).

43 Irvine, J. T., Sinclair, D. C. & West, A. R. Electroceramics: characterization by impedance spectroscopy. *Adv. Mater.* **2**, 132-138 (1990).

44 Maier, J. Defect chemistry and ionic conductivity in thin films. *Solid State Ionics* **23**, 59-67 (1987).

45 Maier, J. Defect chemistry and conductivity effects in heterogeneous solid electrolytes. *Journal of The Electrochemical Society* **134**, 1524 (1987).

46 Sata, N., Eberman, K., Eberl, K. & Maier, J. Mesoscopic fast ion conduction in nanometre-scale planar heterostructures. *Nature* **408**, 946-949 (2000).

47 Wang, S., Liu, Y. & Mo, Y. Frustration in Super-Ionic Conductors Unraveled by the Density of Atomistic States. *Angew. Chem.* **135**, e202215544 (2023).

48 Zhu, Y., He, X. & Mo, Y. First principles study on electrochemical and chemical stability of solid electrolyte–electrode interfaces in all-solid-state Li-ion batteries. *J. Mater. Chem. A.* **4**, 3253-3266 (2016).

49 Nolan, A. M., Liu, Y. & Mo, Y. J. A. E. L. Solid-state chemistries stable with high-energy cathodes for lithium-ion batteries. *ACS Energy Lett.* **4**, 2444-2451 (2019).

50 Kochetkov, I. *et al.* Different interfacial reactivity of lithium metal chloride electrolytes with high voltage cathodes determines solid-state battery performance. *Energy Environ. Sci.* **15**, 3933-3944, doi:10.1039/d2ee00803c (2022).

51 Kresse, G. & Furthmüller, J. Efficient iterative schemes for ab initio total-energy calculations using a plane-wave basis set. *Physical review B* **54**, 11169 (1996).

52 Blöchl, P. E. Projector augmented-wave method. *Physical review B* **50**, 17953 (1994).

53 Perdew, J. P., Ernzerhof, M. & Burke, K. Rationale for mixing exact exchange with density functional approximations. *The Journal of chemical physics* **105**, 9982-9985 (1996).

54 Jain, A. *et al.* Commentary: The Materials Project: A materials genome approach to accelerating materials innovation. *APL Mater.* **1**, 011002 (2013).

55 Shuichi, N. Constant temperature molecular dynamics methods. *Progress of Theoretical Physics Supplement* **103**, 1-46 (1991).

56 He, X., Zhu, Y., Epstein, A. & Mo, Y. Statistical variances of diffusional properties from ab initio molecular dynamics simulations. *Npj Computational Materials* **4**, 1-9 (2018).

57 Momma, K. & Izumi, F. VESTA 3 for three-dimensional visualization of crystal, volumetric and morphology data. *J. Appl. Crystallogr.* **44**, 1272-1276 (2011).

58 Zhu, Y., He, X. & Mo, Y. Origin of Outstanding Stability in the Lithium Solid Electrolyte Materials:

Insights from Thermodynamic Analyses Based on First-Principles Calculations. *ACS Appl. Mater. Interfaces* **7**, 23685-23693, doi:10.1021/acsami.5b07517 (2015).

59 Zhu, Y. Z., He, X. F. & Mo, Y. F. Strategies Based on Nitride Materials Chemistry to Stabilize Li Metal Anode. *Adv. Sci.* **4**, 1600517, doi:Artn 1600517

10.1002/Advs.201600517 (2017).

60 Zhu, Y. Z., He, X. F. & Mo, Y. F. First principles study on electrochemical and chemical stability of solid electrolyte-electrode interfaces in all-solid-state Li-ion batteries. *J. Mater. Chem. A* **4**, 3253-3266, doi:10.1039/c5ta08574h (2016).

61 Wang, S. *et al.* Lithium chlorides and bromides as promising solid-state chemistries for fast ion conductors with good electrochemical stability. *Angew. Chem., Int. Ed. Engl.* **58**, 8039-8043 (2019).

62 Toby, B. H. & Von Dreele, R. B. GSAS-II: the genesis of a modern open-source all purpose crystallography software package. *J. Appl. Crystallogr.* **46**, 544-549 (2013).

63 Farrow, C. *et al.* PDFfit2 and PDFgui: computer programs for studying nanostructure in crystals. *J. Phys. Condens. Matter* **19**, 335219 (2007).

64 Ravel, B. & Newville, M. ATHENA, ARTEMIS, HEPHAESTUS: data analysis for X-ray absorption spectroscopy using IFEFFIT. *J. Synchrotron Radiat.* **12**, 537-541, doi:10.1107/S0909049505012719 (2005).